

Superconducting Edge Contact and Quantum Interference Between Two-Dimensional van der Waals and Three-Dimensional Conventional Superconductors

Michael R. Sinko,¹ Sergio C. de la Barrera,¹ Olivia Lanes,² Kenji Watanabe,³
Takashi Taniguchi,³ David Pekker,² Michael Hatridge,² and Benjamin M. Hunt^{1,*}

¹*Department of Physics, Carnegie Mellon University, Pittsburgh, PA 15213*

²*Department of Physics and Astronomy, University of Pittsburgh, Pittsburgh, PA 15260*

³*Advanced Materials Laboratory, National Institute for Materials Science, Tsukuba, Ibaraki 305-0044, Japan*

Two-dimensional (2D) transition-metal dichalcogenide (TMD) superconductors have unique and desirable properties for integration with conventional superconducting circuits. These include the ability to form atomically-flat and clean interfaces with stable tunnel barriers, increased kinetic inductance due to the atomically-thin geometry, and resilience to very high in-plane magnetic fields [1–5]. However, integration of 2D TMD superconductors in conventional superconducting circuits, particularly those employing microwave drive and readout of qubits, requires that a fully superconducting contact be made between the 2D material and a three-dimensional (3D) superconductor. Here, we present an edge contact method for creating zero-resistance contacts between 2D NbSe₂ and 3D aluminum [6]. These hybrid Al-NbSe₂ Josephson junctions (JJs) display a Fraunhofer response to magnetic field with micron²-scale effective areas as the thin NbSe₂ allows field to uniformly penetrate the flake [7]. We present a model for the supercurrent flow in a 2D-3D superconducting structure by numerical solution of the Ginzburg-Landau equations and find good agreement with experiment. The devices formed from 2D TMD superconductors are strongly influenced by the geometry of the flakes themselves as well as the placement of the contacts to bulk 3D superconducting leads. These results demonstrate our ability to graft 2D TMD superconductors and nano-devices onto conventional 3D superconducting materials, opening the way to a new generation of hybrid superconducting quantum circuits.

Superconducting circuits are ubiquitous in the fields of quantum information and quantum sensing. These circuits are typically fabricated by deposition of metallic superconductors such as Al, Nb, or NbTiN, and most state-of-the-art superconducting qubits use Josephson junctions whose tunnel barriers are created by in-situ oxidation of aluminum electrodes [8, 9]. Despite well-controlled processes for creating Josephson junctions, the oxide barrier thickness varies on the atomic scale, leading to highly non-uniform supercurrent distributions [10]. Oxide barriers can also age as oxygen atoms diffuse out from the oxide, changing the normal state resistance of the junction and hence its critical current [11], which can also result from the absorption or desorption of other atoms or molecules [10, 12, 13]. Despite these limitations, Josephson junction-based superconducting circuits are at the vanguard of quantum computing, used as state-of-the-art qubits but also employed in readout cavities, filters, amplifiers, and circulators. This is enabled by the ability to engineer desired nonlinear Hamiltonians by varying their size by several orders of magnitude, and by embedding junctions in a superconducting loop to form Superconducting QUantum Interference Devices (SQUIDs), as well as related variants such as Superconducting Low-inductance Undulatory Galvanometers (SLUGs), Superconducting Nonlinear Asymmetric Inductive Elements (SNAILs), and Josephson Ring Modulators (JRMs) [8, 9, 14–16].

Two-dimensional vdW superconductors, such as 2H_a-NbSe₂ and 2H_a-TaS₂ [3, 4] (hereafter NbSe₂ and TaS₂), offer complementary properties that leverage their atomic thinness and unique magnetic properties. For example, kinetic inductance $L_{/rmK}$, which results from the inertia of the charge carriers and is inversely proportional to cross-sectional area, can

be quite large in a vdW superconductor because the atomic thinness minimizes the cross-sectional area for a given channel width. A large kinetic inductance is desirable when fabricating superinductors for superconducting circuits like fluxonium qubits, or inductive shunts [17, 18]. Additionally, NbSe₂ and TaS₂ can be readily incorporated in heterostructures in which hexagonal boron nitride (hBN) or the semiconducting transition-metal dichalcogenides (TMDs) could replace oxides as stable and atomically-flat tunnel barriers [19–22]. They also possess strong spin-orbit coupling, which leads to exceptionally high in-plane upper critical fields in few-layer devices [3, 5].

In order to take advantage of the extraordinary properties of 2D van der Waals superconductors, the most promising pathway is to integrate components built from 2D superconductors into larger circuits fabricated using conventional 3D superconducting materials. The *sine qua non* of creating such a hybrid circuit is to create reliable, transparent and robust superconducting contact between the 2D vdW and 3D conventional materials, minimizing dissipation and allowing the use of standard microwave drive and readout techniques. In this work, we present such a method, demonstrating zero-resistance contacts between 2D NbSe₂ and 3D aluminum. In addition, we study the magnetic-flux response of devices having both two-terminal (3D-2D-3D) and SQUID geometries. With the aid of numerical solutions of the Ginzburg-Landau equations, we elucidate how the response of 2D-3D superconducting devices to magnetic field depends strongly on the geometry of the 2D flake because of the gradual variation of the screening currents in two dimensions.

We begin by describing our fabrication methods. Using exfoliation and standard dry-transfer techniques for stacking van

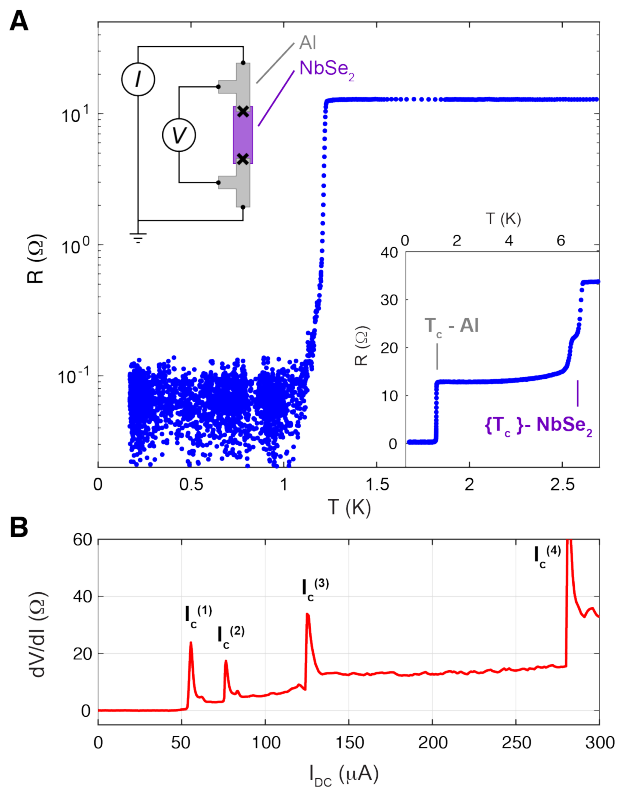


FIG. 1. Zero-resistance contact between few-layer NbSe₂ and aluminum. (A) Semilogarithmic plot of $R(T)$ showing a zero-resistance state, limited by the noise floor of roughly 135 m Ω , in sample F. Inset (bottom-right): linear plot of $R(T)$ showing the Al and two NbSe₂ transitions. Inset (top-left) 4-pt measurement setup for isolating and measuring the contact resistances of the Al/NbSe₂ edge contacts (Al:gray NbSe₂:purple). NbSe₂ is approximately $1.5\ \mu\text{m} \times 3.5\ \mu\text{m}$ and 10 nm thick (see Table I). A lower noise floor of 30 m Ω can be seen in sample A, shown in S6. (B) Differential resistance (dV/dI) vs. DC current I_{DC} of same device, showing four DC critical currents 1 through 4 with $I_c \approx 55, 75, 125, 280\ \mu\text{A}$. The temperature dependence of $I_c^{(3)}$ and $I_c^{(4)}$ (Fig. S2) identifies them as bulk aluminum and NbSe₂ respectively; $I_c^{(1)}$ and $I_c^{(2)}$ are oscillatory in magnetic field and are therefore associated with the Al/NbSe₂ contacts (see Fig. 2).

der Waals materials inside a nitrogen-filled glove box [23], we encapsulate few-layer NbSe₂ above and below with hexagonal boron nitride (hBN). We make contact to the NbSe₂ using evaporated aluminum with no intermediate (adhesion) layer, using a variation on the “edge contact” method [6]. Briefly, we expose the edge of the NbSe₂ to be contacted by reactive-ion etching through all three layers of the hBN-NbSe₂-hBN stack. We then transfer the stack immediately into an evaporation chamber for an argon ion mill process, to clean the exposed cross section of the stack, after which we tilt the sample *in situ* in the appropriate orientation to evaporate Al onto the exposed NbSe₂ edge (Fig. S1). We have successfully made devices using both single- and double-angle evaporation.

A schematic of the two-terminal (3D-2D-3D) device is

shown in the inset to Fig. 1A. In the pseudo-four-terminal measurement configuration shown, the measured resistance $R(T)$ is the series resistance of the 2D NbSe₂ flake, the resistance of the aluminum-NbSe₂ interface, and the 3D aluminum leads between the interface and the voltage probes. This measurement configuration allows us to eliminate resistances from the voltage and current leads, but includes the interface resistance between the 3D and 2D superconductors. Fig. 1A shows a measurement of $R(T)$ between 2.5 K and the 175 mK in a dilution refrigerator. The transition at 7 K is that of the NbSe₂ flake, whose T_c matches the bulk value of NbSe₂, indicating that the sample is more than 6 layers thick [24]. A second transition occurring at 6.5 K is also associated with the NbSe₂ flake, as the critical current of this suppressed T_c merges with that of the 7 K transition as $T \rightarrow 0$ (Fig. S5). A final transition occurs at 1.2 K, which we attribute to the deposited aluminum leads as well as the Al/NbSe₂ contacts. Below this final transition, the total resistance of the device, including the Al-NbSe₂ junctions, has dropped to zero within the noise floor of our measurement ($R < 10^{-1}\ \Omega$). We filter each measurement line using both low-pass RC filters ($f_{3\text{dB}} \approx 10\ \text{kHz}$) and radiofrequency filters mounted on the mixing chamber stage of the dilution refrigerator (Fig. S7), which have been shown to be particularly important for studies of two-dimensional superconductors [25].

In Figure 1B, we plot a measurement of the differential resistance (dV/dI) as a function of the DC current I_{DC} passing through the device. We observe four critical currents, of which the lower two show periodic modulations with applied magnetic field (see Fig. 2) while the larger two currents decrease monotonically with applied field (S3). This distinction associates the smaller two critical currents with the Al/NbSe₂ interfaces, which appear to form Josephson junctions, and the larger two critical currents with the bulk Al and NbSe₂. We can further distinguish the bulk Al and NbSe₂ critical currents by their magnetic field and temperature dependences (see Supplementary Information).

The two NbSe₂-Al contacts in this sample are slightly different in size (Table IF and Fig. 2C), so we associate the narrower contact with $I_c^{(1)} = 55\ \mu\text{A}$ and the wider contact with $I_c^{(2)} = 75\ \mu\text{A}$, resulting in critical current densities $J_c^{(1)} = 3.9 \times 10^9\ \text{A/m}^2$ and $J_c^{(2)} = 3.75 \times 10^9\ \text{A/m}^2$. We estimate that >60% of (approximately 8-10) fabricated devices have a resistance of 0.2 Ω or less in the limit of $T \rightarrow 0$. The remaining devices have residual $T \rightarrow 0$ resistances that range from a few Ω up to 81 Ω . We have not conclusively identified the origin of the non-zero resistances in some devices, but as we have improved our device fabrication procedures, particularly the *in-situ* ion milling immediately prior to Al evaporation, the yield of $R = 0$ devices has increased and has also resulted in consistently higher critical current densities.

To gain insight into the nature of the 2D-3D superconducting interface, we studied the response of these two-terminal 3D-2D-3D devices to magnetic flux perpendicular to the plane of the 2D NbSe₂ flake. In Fig. 2D, we plot the differential re-

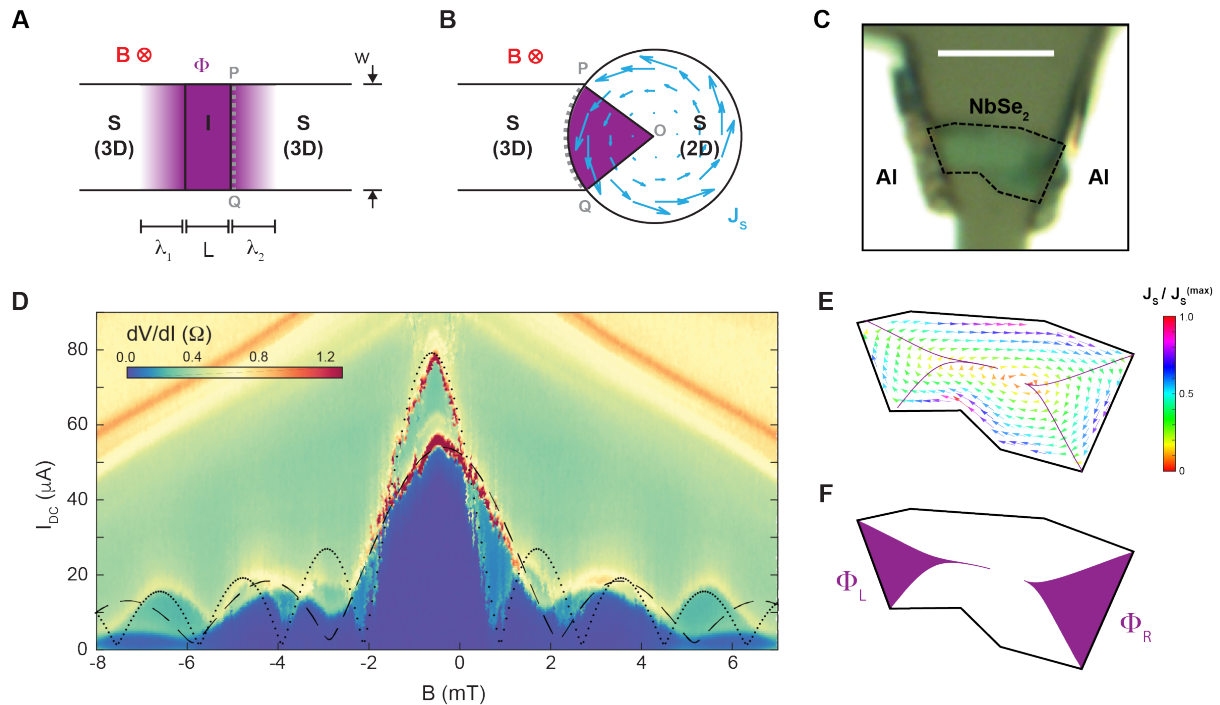


FIG. 2. **Quantum interference in a two-terminal NbSe₂-aluminum device.** (A) Model of a 3D-3D Josephson junction. The phase change from P to Q (along the thick dashed line) is 2π when one Φ_0 of flux is threaded through the area depicted in magenta. The effective area of the JJ is $w \cdot (L + \lambda_1 + \lambda_2)$. (B) Model of a 2D-3D JJ. The 2D flake is depicted in a circular geometry, for simplicity. In response to a field \mathbf{B} , circulating supercurrent \mathbf{J}_s (blue arrows) flows in the 2D bulk. As with the 3D-3D JJ, the phase change from P to Q along the dashed line (at the 2D-3D interface) is 2π , which requires the phase change along a contour interior to the 2D flake to be zero and therefore to be perpendicular to \mathbf{J}_s everywhere. This is satisfied by the wedge-shaped contour \overline{POQ} , and thus the effective area of the 2D-3D JJ is enclosed by the pie-shaped area shown in magenta. (C) Optical image of device F. Scale bar is 4 μm . (D) dV/dI as a function of I_{DC} and B for device F. Two superimposed single-junction I_0 vs. flux responses are clearly visible. Theoretical $I_c(B)$ curves (black dotted and dashed lines) are overlaid on the data, corresponding to the two contacts (see main text). The only input to the theory is the 2D flake shape (shown in C, E, F); the calculated fluxes Φ_L and Φ_R (see panel F) are used to plot the theoretical $I_c(B)$ with 8% scaling along the B -axis. The orange feature in the data is the bulk critical current of Al. (E) Calculated supercurrent distribution \mathbf{J}_s and (F) effective fluxes Φ_L and Φ_R associated with the left and right contacts of device F. Within the 2D flake, the contours bounding Φ_L and Φ_R are everywhere perpendicular to \mathbf{J}_s .

sistance of such a device as a function of DC current I_{DC} and B . The data appear to display two interference patterns, each with a larger central peak and several smaller satellite peaks. This strongly suggests that we are measuring the individual responses from each junction, which is supported by our observation that in sequential data sets similar to Fig. 2D, we have observed one set of peaks shifting relative to the other, which likely resulted from the depinning of trapped flux at one of the contacts (Fig. S2).

The two superimposed interference patterns each resemble the $I_c(B)$ of a single Josephson junction, which, in a typically 3D-3D superconducting JJ, is proportional to $|\sin(x)/x|$ with $x = \pi B A_{\text{JJ}} / \Phi_0$ the flux penetrating the small area $A_{\text{JJ}} = w \cdot \ell_{\text{eff}}$ of the JJ (Fig. 2A), where w is the width of the junction and $\ell_{\text{eff}} = L + \lambda_1 + \lambda_2$ is given by the physical length L plus the penetration depths on either side of the junction, λ_1 and λ_2 . Here, $\Phi_0 = h/2e$ is the superconducting flux quantum. In our 2D-3D interference data, the periods of oscillation ΔB_i are approximately 2 mT and 4 mT for the two interfer-

ence patterns, corresponding to JJ areas $A_i = \Phi_0 / \Delta B_i$ of 1 μm^2 and 0.5 μm^2 respectively, which are significantly larger than the equivalent physical area produced by the edge contact method [6, 16].

We seek a more sophisticated understanding of the interference patterns. To this end, we note first that in a 2D superconductor of thickness $d \ll \lambda$, where λ is the bulk penetration depth, the magnetic flux nearly uniformly penetrates the superconductor because the relevant length scale for the screening of the applied field is the Pearl length $\lambda_{\text{Pearl}} = 2\lambda^2/d$ [7, 26]. λ_{Pearl} can exceed the size of the sample for very thin flakes. This means that in comparison to the 3D-3D JJ, the effective area penetrated by the flux must be much larger in the 2D-3D junction, and the contour around which the superconducting phase winds by 2π is determined by the specific flow pattern of the supercurrent \mathbf{J}_s in the 2D flake (Fig. 2B). The portion of this contour in the 2D flake is thus unique, giving rise to a strong sensitivity of the interference pattern to the precise shape and size of the 2D flake as well as to the

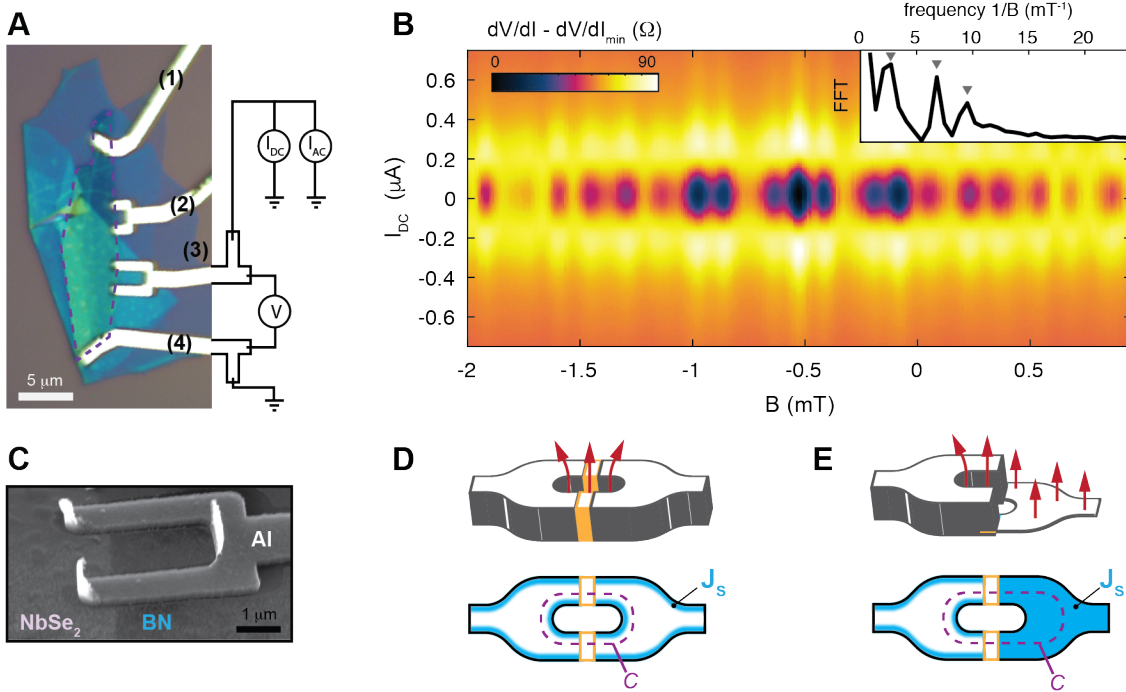


FIG. 3. Quantum interference in a 2D-3D NbSe₂-aluminum SQUID. (A) Optical image and measurement schematic of device C. The NbSe₂ flake is outlined in a dashed purple line. Differential resistance (dV/dI) was measured using the bottom two contacts, numbered 3 and 4 (indicated by the measurement schematic) while the top two contacts (1 and 2) were floating. (B) Quantum interference pattern observed in device C at 30 mK. A minimum resistance of $(dV/dI)_{\min} = 81$ ohms has been subtracted from the data. Data for a second SQUID device (B) that show a true zero resistance as $T \rightarrow 0$ are shown in Fig. S8. Inset: Fast Fourier transform (FFT) amplitude of a linecut along $I_{DC} = 0$. The three frequencies, indicated by arrows, are $1/\Delta B_i = 2.7, 6.8,$ and 9.5 mT^{-1} (corresponding respectively to areas $S_i = \Phi_0/\Delta B_i = 5.4, 13.6,$ and $19.1 \mu\text{m}^2$). (C) Tilted SEM image of the SQUID loop (3) in device C formed by two Al edge contacts to the NbSe₂ flake encapsulated by BN on an SiO₂ substrate. (D) Schematic cross-section of a 3D-3D SQUID. Supercurrent \mathbf{J}_s flows in a layer of width $\sim \lambda$ from the surface. The contour C used to calculate the fluxoid quantization in the device can be chosen deep in the interior of the superconductor such that $\oint_C \mathbf{J}_s \cdot d\mathbf{l} = 0$. (E) Schematic cross-section of a 2D-3D SQUID. Since \mathbf{J}_s is non-zero everywhere in the 2D layer, C cannot be chosen arbitrarily in the 2D bulk, which results in a larger effective area that determines the periodicity of critical-current oscillations.

placement of the 3D leads.

We constructed a theoretical model for the flow of supercurrent \mathbf{J}_s in our device, based on numerical solutions of the Ginzburg-Landau equations (see Methods), in order to understand quantitatively the shorter oscillation periods (larger areas) seen in the Fig. 2 data. We emphasize that the only input to our numerical model is the precise shape (to scale) of the 2D NbSe₂ flake. The results of the simulation for both contacts are shown in Fig. 2E and F, and the $I_c(B)$ for both contacts are superimposed on the data in Fig. 2D. With only the dimensions of the flake as an input parameter, our simple model does quite a good job of explaining the critical currents: the ratio of the central peak to the satellite peaks is quite accurate, and the predicted areas are within about 8% of the values measured in the experiment. Additionally, our model predicts that the critical currents do not reach zero, a feature of the experimental data as well. Critical current zeroes occur when forward and backward supercurrents across the junction perfectly cancel each other, which can only happen for flakes that have a mirror symmetry with respect to a line perpendicular

to the Josephson junction that bisects the junction into two equal segments. As our flakes lack such a symmetry, we do not expect to see critical current zeroes. Agreement between simulation and experiment on this point might be improved if we relaxed our assumption of uniform Josephson coupling along the interface.

In order to further investigate quantum interference in the presence of near-uniform flux penetration in the 2D bulk, we prepared devices having the geometry of a SQUID, depicted in Fig. 3A,C. Using the circuit shown in Fig. 3A, to measure between the bottommost Al lead (#4) and the larger-area SQUID lead immediately above it (#3), displayed in Fig. 3C, we sweep the applied magnetic field and observe a periodic oscillation in the critical current of the SQUID (Fig. 3B,D). The oscillation in the critical current in our 2D-3D SQUID exhibits a pattern that is distinct from a conventional 3D-3D SQUID formed by joining two 3D superconductors. In a conventional 3D-3D SQUID, the critical current has a periodicity in magnetic field ΔB determined by the physical area S enclosed by the SQUID, namely $\Delta B = \Phi_0/S$. The critical

current of a SQUID depends on the flux $\Phi = BS$ and supercurrent \mathbf{J}_s

$$\frac{I_c(\Phi)}{I_{c,\max}} = \left| \cos \left(\pi \frac{\Phi}{\Phi_0} + \Lambda \int_{C'} \mathbf{J}_s \cdot d\ell \right) \right|, \quad (1)$$

where $\Lambda = m/n_s e$ and the contour C' excludes the small physical length of the two JJs. In the 3D-3D SQUID, the contour C' can typically be chosen in the interior of the 3D superconductor such that $\mathbf{J}_s = 0$ and the periodicity of $I_c(B)$ is determined solely by the physical area S (Fig. 3D). This oscillatory pattern is typically modulated by the Fraunhofer pattern due to the flux response of the individual junctions, which has a much longer period corresponding to their much smaller physical sizes. In Fig. 3B it appears that there are oscillations at multiple frequencies $1/\Delta B_i$ whose associated areas $S_i = \Phi_0/\Delta B_i$ are much closer together than would be expected from the ratio of the physical SQUID area to the physical Josephson junction area. A Fourier transform of the data in Fig. 3B reveals that there are three frequencies $1/\Delta B_i = 2.7, 6.8, \text{ and } 9.5 \text{ mT}^{-1}$, which correspond respectively to areas $S_i = \Phi_0/\Delta B_i = 5.4, 13.6, \text{ and } 19.1 \mu\text{m}^2$. None of these precisely match the physical area of the SQUID shown in detail in Fig. 3C ($7 \mu\text{m}^2$) and, as mentioned above, the beating pattern is inconsistent with the ratio of SQUID area to Josephson junction area.

We employed our theoretical model to calculate the larger effective areas of both contact #4 and the SQUID-shaped contact #3. Analogous to the larger effective area of the 2D-3D Josephson junctions studied in Fig. 2, the effective area S_{eff} of the SQUID, bounded by the unique contour around which the superconducting phase winds by 2π , is larger than that of the physical area due to the contribution of non-zero \mathbf{J}_s flowing in the bulk of the 2D flake (Equation 1 and Fig. 3F). We find that the effective SQUID area at contact #3 is $S_{\text{eff}} = 19.7 \mu\text{m}^2$, which is very close to the experimentally determined value of $19.1 \mu\text{m}^2$, calculated from the largest frequency, $1/\Delta B = 9.5 \text{ mT}^{-1}$ in the Fourier transform. Contact #4 should behave as a 2D-3D Josephson junction with a large effective area, as for the two-terminal device in Fig. 2; indeed, our simulation predicts $S_{\text{eff}} = 6.3 \mu\text{m}^2$, which corresponds to the lowest observed frequency $1/\Delta B = 2.7 \text{ mT}^{-1}$ ($5.4 \mu\text{m}^2$). Our observation of a third frequency has no straightforward explanation using our model, but may have to do with coupling between phase slips on the two junctions, mixing the frequencies and giving rise to additional sum/difference frequencies. We also performed this analysis for a second SQUID device (C) for which the data are shown in Fig. S8.

In conclusion, we have shown that robust superconducting edge contacts can be made between encapsulated 2D TMD intrinsic superconductors and conventionally evaporated 3D metals. These contacts form Josephson junctions between two dissimilar superconductors, whose oscillation period in the $I_c(B)$ Fraunhofer pattern suggests that the effective areas of the Josephson junctions are significantly larger than the expected areas, an observation which also holds for devices having SQUID geometries. The $\sim \mu\text{m}^2$ effective areas of the

Josephson junctions suggests that they may be useful in applications involving compact magnetometer arrays or in scanned probes, because of the high ratio of flux-sensitive area to physical device area. These 2D-3D superconducting contacts lay the foundation of a technological pathway to integrate 2D superconductors and heterostructures as components in conventional superconducting circuits. With further refinement, and using our theoretical model to inform the design, the Josephson junctions and SQUIDs fabricated using this methodology could be used as circuit components in and of themselves, in addition to bridging the 2D-3D divide to incorporate fully 2D circuit components.

METHODS

Device fabrication

We fabricate devices by exfoliating ~ 10 -micron-long flakes from a bulk crystal of 2H-NbSe₂ sourced from HQ Graphene. Unlike graphene, which is hBN encapsulated for superior electronic properties, intrinsically superconducting TMDs are air or water vapor sensitive and begin to degrade in an ambient environment. This necessitates the encapsulation of NbSe₂ by hBN using standard dry transfer techniques in an inert N₂ glovebox environment to prevent the degradation of the air sensitive NbSe₂. After a PMMA/MMA bilayer resist mask is patterned using e-beam lithography, an initial etch is made with CHF₃/O₂ in a reactive ion etching system. The sample is examined and then sealed in an inert environment until it is loaded into a Plassys 8-Pocket e-gun evaporator with ion gun. An initial 3-minute, high-power Ar ion mill step is used to clean and expose fresh surfaces on the exposed cross-sections of the heterostructure, then the substrate is rotated to an angle $\pm 30^\circ$ from perpendicular to the direction the evaporation. This angle ensures thorough coverage of the exposed NbSe₂ cross section by the Al, evaporated at 0.3 nm/s. Al is evaporated to ensure uniform coverage of heterostructures that range from 30 – 60 nm, devices with leads facing opposite directions have 40 nm deposited while the sample is tilted to one side, and then another 40 nm of Al deposited while it is tilted the opposite direction.

Magnetotransport measurements

Magnetotransport measurements were performed using standard low-frequency AC lock-in techniques with an SR860 lock-in amplifier and a Keithley 2400 SMU. The samples were measured in a dilution refrigerator to a minimum temperature of 40 mK in fields up to 5T. Fig. 1c shows the measurement setup in which each superconducting lead that connects to the NbSe₂ flake splits in two, enabling a 4-pt resistance measurement that would isolate any remaining contact resistance after both the Al lead and NbSe₂ flake have transitioned to superconducting states. A series of filters were used to isolate the

sample from high frequency noise, including a low-pass RC filter, Cu tape GHz filters and a Cu clamshell enclosure, serving as a Faraday cage to encase and isolate the sample [27–31]. These filters block higher frequency noise that drives the contact out of the superconducting state, creating a residual resistance [27]. dV/dI measurements were taken by the sweeping the sourced DC current at stepped field intervals to form the colorplot in Fig. 3B.

Theoretical model

In this section we build a model for the dependence of the Josephson current between the aluminum leads and the NbSe₂ flake, similar in spirit to Ref. [32]. We make the assumption that the Josephson energy E_J of the contact between the leads and the flake is much lower than the energy of the screening supercurrents induced by the magnetic field in the flake. For a JJ with $I_c = 75 \mu\text{A}$, $E_J = \Phi_0 I_c / 2\pi \approx 150 \text{ meV}$. The energy of the screening supercurrents is roughly two orders of magnitude higher, with the reasonable assumptions that the (2D) superfluid density is $n_s \sim 10^{15} \text{ cm}^{-2}$ and that the phase gradient in the sample is of the order of $2\pi/L$, where $L \sim 2 \mu\text{m}$ is a linear dimension of the 2D sample. This assumption significantly simplifies our analysis as we can first build a model of the supercurrents in the flake and then use the output of this model to obtain the Josephson currents.

Our starting point for describing the supercurrents in the flake is the Ginzburg-Landau equation

$$\alpha\psi + \beta|\psi|^2\psi + \frac{1}{2m^*} \left(\frac{\hbar}{i} \vec{\nabla} - \frac{2e}{c} \vec{A} \right)^2 \psi = 0, \quad (2)$$

where ψ is the complex order parameter, \vec{A} is the gauge field, m^* is the mass of a Cooper pair, and α and β the Landau-Ginzburg parameters. For small superconductors (such that the linear size of the 2D sample is much smaller than the Pearl penetration depth) the magnetic field completely penetrates the superconductor, and hence one can ignore the variations in the magnitude of ψ . Therefore, we express the order parameter ψ in terms of a (constant) amplitude ψ_0 and a position dependent phase $\phi(\vec{r})$: $\psi(\vec{r}) = \psi_0 e^{i\phi(\vec{r})}$. Using this form of the order parameter, the Ginzburg-Landau equation becomes

$$\vec{\nabla}^2 \phi(\vec{r}) - \frac{2e}{\hbar c} \vec{\nabla} \cdot \vec{A}(\vec{r}) = 0. \quad (3)$$

The supercurrents are given by

$$\vec{J}(\vec{r}) = \frac{2e\hbar}{m^*} \psi_0^2 \left(\vec{\nabla} \phi(\vec{r}) - \frac{2e}{\hbar c} \vec{A}(\vec{r}) \right). \quad (4)$$

To obtain the current distribution in the flake we numerically solve equation Eq. 3 subject to the boundary condition that there is no supercurrent across the boundary, i.e. $\vec{J} \cdot \vec{n}|_{\partial} = 0$ where \vec{n} is the unit normal vector on the boundary. We note that in principle the current across the boundary should be non-zero in the regions of contact between the flake and the

aluminum leads. We ignore this contribution following our assumption of weak Josephson currents. We also note that as Eq. 3 (supplemented by the boundary conditions) is linear $\phi(\vec{r}) \propto B_z$, and hence it is sufficient to obtain $\phi(\vec{r})$ for a single value of B_z and then scale the resulting solution.

To obtain numerical solutions, we wrote a Mathematica script which allows us to trace the shape of the flake and convert it to into a partial differential equation for $\phi(\vec{r})$ supplemented by Neumann boundary conditions (we use the Landau gauge $\vec{A}(\vec{r}) = B_z x \hat{e}_y$). The computed supercurrents in the flake are plotted in Fig. 3.

To compute the Josephson current between the i -th lead and the flake we define the phase

$$\chi = \varphi + \int dl \left(\vec{\nabla} \phi(\vec{r}) - \frac{2e}{\hbar c} \vec{A}(\vec{r}) \right), \quad (5)$$

where φ is the superconducting phase associated with the flake and the integral runs around the boundary of the flake. The Josephson current between the i -th lead and the flake is given by

$$J_i = J_c \int_{\text{contact}} dl \sin(\phi_i - \chi), \quad (6)$$

where J_c is the critical current density, ϕ_i is the superconducting phase of the i -th lead, and the line integral runs over the points at which the lead makes contact with the flake.

CONTRIBUTIONS

M.R.S. fabricated the devices with assistance from O.L. M.R.S., S.C.B., and B.M.H. performed the magnetotransport measurements. D.P. performed the numerical modelling of the samples and K.W. and T.T. grew the hBN crystals. M.R.S. and B.M.H. wrote the paper. M.H. and B.M.H. supervised the work, and all authors reviewed and commented on the manuscript.

ACKNOWLEDGEMENTS

Work on device fabrication and measurement by M.R.S. and O.L. was supported by the National Science Foundation PIRE program under award number 1743717. B.M.H. acknowledges support by the Department of Energy under the Early Career award program (DE-SC0018115). S.C.B. was supported by the Department of Energy (DE-SC0018115) for measurements of the superconducting devices. B.M.H. and S.C.B. acknowledge support in the early stages of this project from the Charles E. Kaufman Foundation, a supporting organization of The Pittsburgh Foundation, via Young Investigator research grant KA2016-85226. The authors acknowledge use of the Materials Characterization Facility at Carnegie Mellon University supported by grant MCF-677785. This work was performed, in part, at the Nanoscale Fabrication and Characterization Facility, a laboratory of the Gertrude E. and John M.

Petersen Institute of NanoScience and Engineering, housed at the University of Pittsburgh. We also thank the Pittsburgh Quantum Institute (PQI) for hosting many productive conversations.

The authors declare no competing interests.

* bmhunt@andrew.cmu.edu

- [1] Kretinin, A. V. *et al.* Electronic Properties of Graphene Encapsulated with Different Two-Dimensional Atomic Crystals. *Nano Letters* **14**, 3270–3276 (2014).
- [2] Rooney, A. P. *et al.* Observing Imperfection in Atomic Interfaces for van der Waals Heterostructures. *Nano Letters* **17**, 5222–5228 (2017).
- [3] Barrera, S. C. d. l. *et al.* Tuning Ising superconductivity with layer and spinorbit coupling in two-dimensional transition-metal dichalcogenides. *Nature Communications* **9**, 1427 (2018).
- [4] Navarro-Moratalla, E. *et al.* Enhanced superconductivity in atomically thin TaS₂. *Nature Communications* **7**, 11043 (2016).
- [5] Xi, X. *et al.* Evidence of Ising pairing in superconducting NbSe₂ atomic layers. *Nature Physics* **12**, 139–143 (2016).
- [6] Wang, L. *et al.* One-Dimensional Electrical Contact to a Two-Dimensional Material. *Science* **342**, 614–617 (2013).
- [7] Pearl, J. Current distribution in superconducting films carrying quantized fluxoids. *Applied Physics Letters* **5**, 65–66 (1964).
- [8] Devoret, M. H. & Schoelkopf, R. J. Superconducting Circuits for Quantum Information: An Outlook. *Science* **339**, 1169–1174 (2013).
- [9] devoret, M. H. & Martinis, J. M. Implementing Qubits with Superconducting Integrated Circuits. *Quantum Information Processing* **3**, 163–203 (2004).
- [10] Zeng, L. J. *et al.* Direct observation of the thickness distribution of ultra thin AlO_x barriers in Al/AlO_x/Al Josephson junctions. *Journal of Physics D: Applied Physics* **48**, 395308 (2015).
- [11] Ambegaokar, V. & Baratoff, A. Tunneling Between Superconductors. *Physical Review Letters* **10**, 486–489 (1963).
- [12] Pop, I. M. *et al.* Fabrication of stable and reproducible sub-micron tunnel junctions. *Journal of Vacuum Science & Technology B, Nanotechnology and Microelectronics: Materials, Processing, Measurement, and Phenomena* **30**, 010607 (2012).
- [13] Scherer, H., Weimann, T., Zorin, A. B. & Niemeyer, J. The effect of thermal annealing on the properties of AlAlO_xAl single electron tunneling transistors. *Journal of Applied Physics* **90**, 2528–2532 (2001).
- [14] Bergeal, N. *et al.* Analog information processing at the quantum limit with a Josephson ring modulator. *Nature Physics* **6**, 296–302 (2010).
- [15] Frattini, N. E., Sivak, V. V., Lingenfelter, A., Shankar, S. & Devoret, M. H. Optimizing the Nonlinearity and Dissipation of a SNAIL Parametric Amplifier for Dynamic Range. *Physical Review Applied* **10** (2018).
- [16] Clarke, J. & Braginski, A. I. (eds.) *The SQUID Handbook: Fundamentals and Technology of SQUIDS and SQUID Systems* (Wiley, 2004), 1 edn.
- [17] Vissers, M. R. *et al.* Frequency-tunable superconducting resonators via nonlinear kinetic inductance. *Applied Physics Letters* **107**, 062601 (2015).
- [18] Annunziata, A. J. *et al.* Tunable superconducting nanoinductors. *Nanotechnology* **21**, 445202 (2010).
- [19] Wang, J. I.-J. *et al.* Coherent control of a hybrid superconducting circuit made with graphene-based van der Waals heterostructures. *Nature Nanotechnology* (2018).
- [20] Lee, K.-H. *et al.* Two-Dimensional Material Tunnel Barrier for Josephson Junctions and Superconducting Qubits. *Nano Letters* (2019).
- [21] Kim, M. *et al.* Strong Proximity Josephson Coupling in Vertically Stacked NbSe₂/Graphene/NbSe₂ van der Waals Junctions. *Nano Letters* **17**, 6125–6130 (2017).
- [22] Kim, K. *et al.* van der Waals Heterostructures with High Accuracy Rotational Alignment. *Nano Letters* **16**, 1989–1995 (2016).
- [23] Tsen, A. W. *et al.* Nature of the quantum metal in a two-dimensional crystalline superconductor. *Nature Physics* **12**, 208–212 (2016).
- [24] Xi, X. *et al.* Ising pairing in superconducting NbSe₂ atomic layers. *Nature Physics* **12**, 139–143 (2016).
- [25] Tamir, I. *et al.* Sensitivity of the superconducting state in thin films. *Science Advances* **5**, eaau3826 (2019).
- [26] Li, T., Gallop, J. C., Hao, L. & Romans, E. J. Josephson penetration depth in coplanar junctions based on 2d materials. *arXiv:1907.12055 [cond-mat]* (2019). ArXiv: 1907.12055.
- [27] Spietz, L., Teufel, J. & Schoelkopf, R. J. A Twisted Pair Cryogenic Filter. *arXiv:cond-mat/0601316* (2006).
- [28] Chong, Y., Song, W., Rehman, M. & Ryu, S.-W. Transmission Properties of Cryogenic Twisted Pair Filters. *Journal of the Korean Physical Society* **57**, 1490–1493 (2010).
- [29] Bluhm, H. & Moler, K. A. Dissipative cryogenic filters with zero dc resistance. *Review of Scientific Instruments* **79**, 014703 (2008).
- [30] Mandal, S. *et al.* Efficient radio frequency filters for space constrained cryogenic setups. *Review of Scientific Instruments* **82**, 024704 (2011).
- [31] Thalmann, M., Pernau, H.-F., Strunk, C., Scheer, E. & Pietsch, T. Comparison of cryogenic low-pass filters. *Review of Scientific Instruments* **88**, 114703 (2017).
- [32] Pekker, D., Bezryadin, A., Hopkins, D. S. & Goldbart, P. M. Operation of a superconducting nanowire quantum interference device with mesoscopic leads. *Physical Review B* **72** (2005).

SUPPLEMENTARY INFORMATION

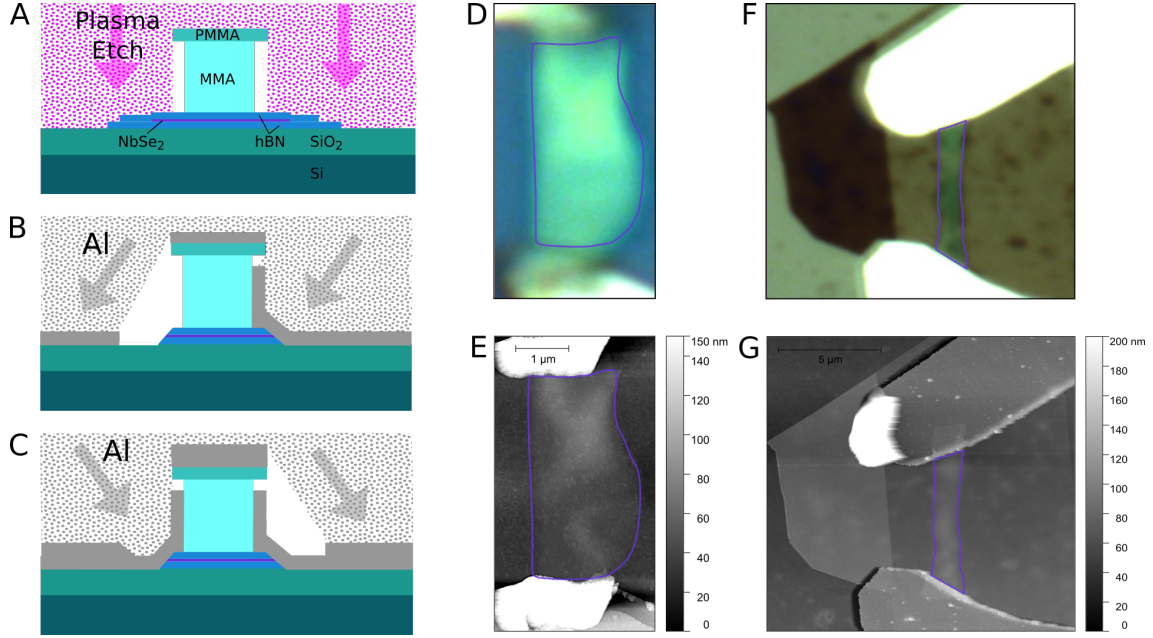


FIG. S1. (A) After the lithographic mask is patterned via EBL, a reactive ion etch is used to expose a cross-section of the hBN/NbSe₂/hBN heterostructure. The stack is then loaded into a Plassys 8 Pocket e-gun Evaporator with ION Gun where a 3 minute Ar ion mill step is used to expose a fresh facet *in situ* before evaporation. (B) Aluminum is evaporated at an angle 30 degrees from vertical. (C) Optionally, additional evaporation angles can be used, but will result in additional aluminum critical currents due to the layering (see Fig. S6B and C). (D/E) Optical and AFM images of sample A. NbSe₂ flake is outlined in purple, scale bar is 1 μm . (F/G) Optical and AFM images of sample D. NbSe₂ flake is outlined in purple, scale bar is 5 μm .

Sample	A	B	C	D	E	F	G
Geometry	2 terminal	SQUID	SQUID	2 terminal	2 terminal	2 terminal	2 terminal
Evaporation	Double angle	Single angle	Single angle	Single angle	Single angle	Single angle	Single angle
Thickness	10 nm, 12.5 nm	11.2 nm	11.3 nm, 17.5 nm	11.5 nm, 12.4 nm	6.2 nm	10 nm	8 nm
Contact width	1 μm , 1.3 μm	2x 1 μm , 8 μm	2x 1 μm , 5.2 μm	1.3 μm , 1.4 μm	1.5 μm , 0.5 μm	1.4 μm , 2.0 μm	1.2 μm , 1.4 μm
I_c	12 μA , 26 μA	10 μA , 40 μA	0.15 μA , 3 μA	70 μA	-	55 μA , 75 μA	108 μA , 128 μA
J_c	$1.2 \times 10^9 \text{ A/m}^2$	$1.67 \times 10^9 \text{ A/m}^2$	$1.3 \times 10^7 \text{ A/m}^2$	$4.7 \times 10^9 \text{ A/m}^2$	-	$3.8 \times 10^9 \text{ A/m}^2$	$1.14 \times 10^{10} \text{ A/m}^2$
$R_{\text{normal}}^{\text{contact}}$	4 Ω	2 Ω	130.6 Ω	12 Ω	-	14 Ω	200 Ω
R_{SC}	$\leq 30 \text{ m}\Omega$	200 m Ω	81.1 Ω	$\leq 30 \text{ m}\Omega$	-	$\leq 130 \text{ m}\Omega$	N/A
$A_{\text{SQUID}}^{\text{physical}}$	N/A	4 μm^2	7 μm^2	N/A	N/A	N/A	N/A
$A_{\text{effective}}$	-	14 μm^2	19 μm^2	-	-	0.5 μm^2 , 1 μm^2	-

TABLE I. Properties of 7 samples exhibiting superconducting contacts. Lateral dimensions are obtained from optical and AFM images, Thicknesses are obtained by AFM topography. Critical current densities are calculated from these dimensions. $R_{\text{normal}}^{\text{contact}}$ is measured in the critical current measurements where the contacts have gone normal, but while the Al and NbSe₂ flake are still superconducting. R_{SC} is measured as $T \rightarrow 0$ with no applied DC current or magnetic field. Effective areas are the outputs from the Ginzburg-Landau model.

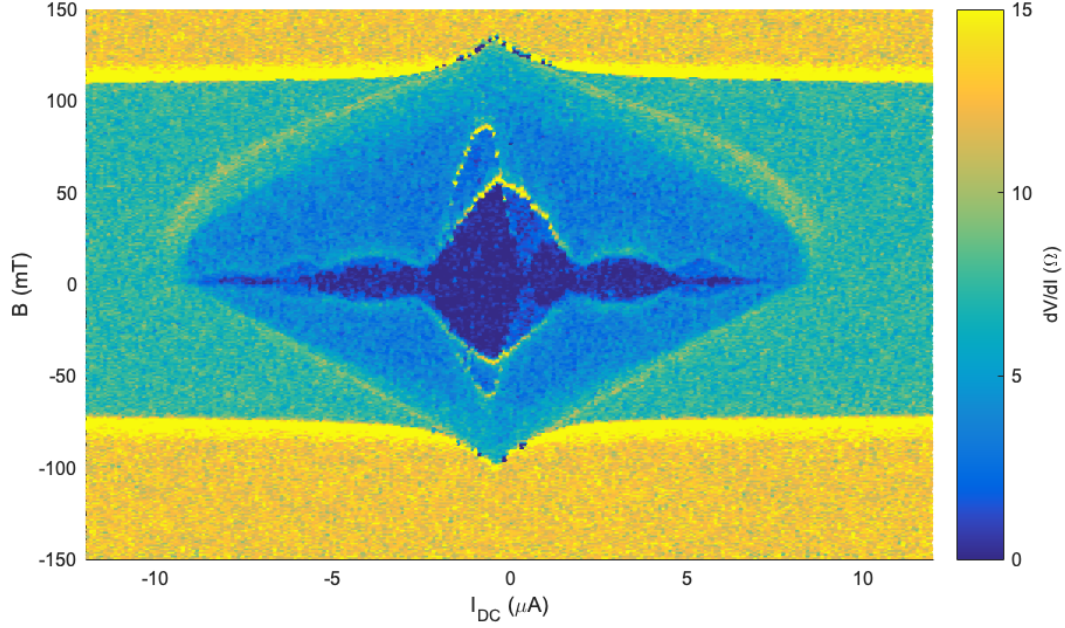


FIG. S2. dV/dI vs. I_{DC} and B (Device F), with larger I_{DC} and B ranges than in Fig. 2A. I_{DC} was swept from negative to positive, resulting in the top/bottom asymmetry. The critical current of the aluminum leads splits at magnetic fields greater than 2 mT, with one component persisting at B fields much greater than the critical field of bulk Al. We attribute this persistent critical current with the narrow regions of the Al leads, where orbital pair breaking effects are slightly suppressed due to the lateral dimensions of the leads ($\sim 1 \mu\text{m}$). An offset between the centers of the Fraunhofer patterns may indicate that there is a difference in the amount of trapped flux within the regions associated with each contact

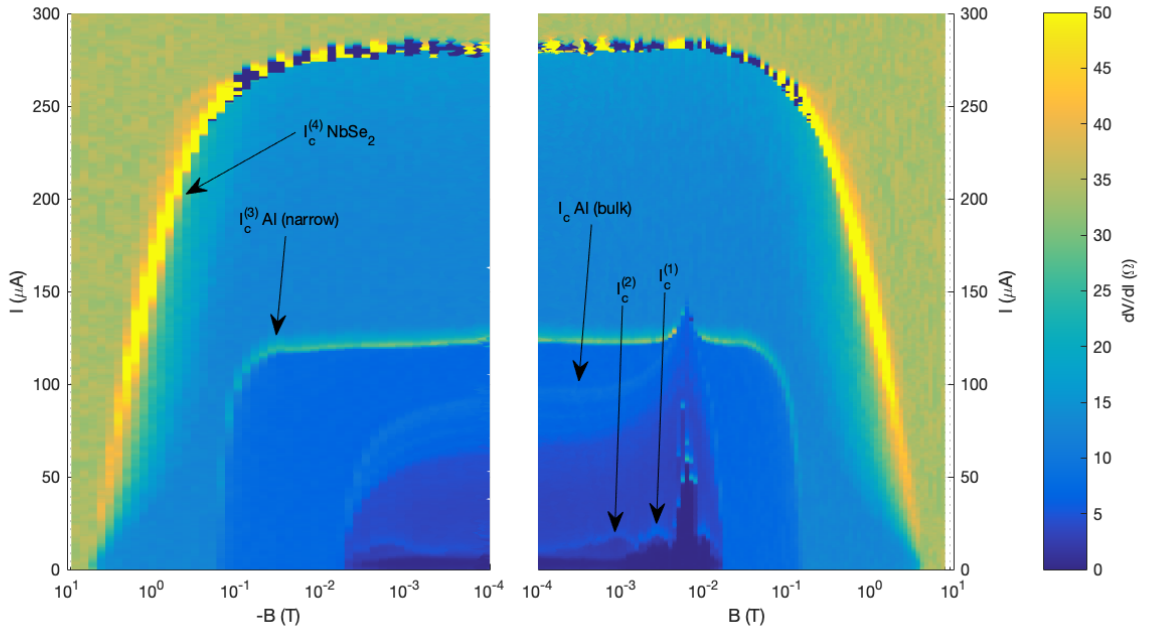


FIG. S3. Plot of dV/dI vs. $\pm \log(B)$ and I_{DC} (Device F). Negative B values are shown on the left in a reversed semilogarithmic plot, leaving a discontinuity between ± 0.1 mT. The center of the Fraunhofer patterns is shifted from zero applied field by 5 mT due to trapped flux, and all critical fields and currents can be observed: Al and Al/NbSe₂ at $H_c \approx \pm 10$ mT, narrow Al leads at an elevated $H_c \approx 150$ mT due to lateral suppression of orbital pair breaking effects, and the NbSe₂ flake at $H_{c2} \approx 4.5$ T

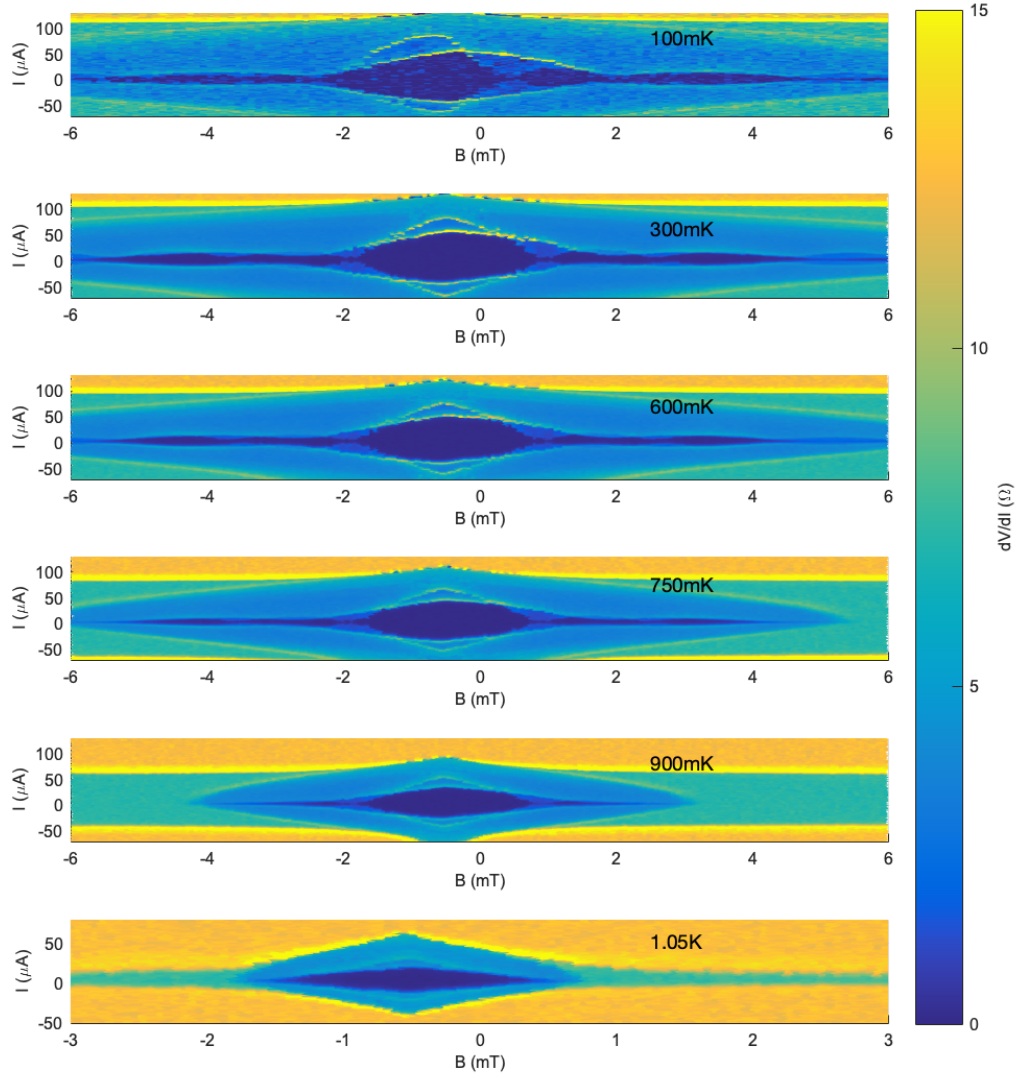


FIG. S4. Fig. S2 is reproduced in the top plot. Temperatures were held stable while I_{DC} and B vs. dV/dI data were obtained for device F. The periodicity of the Fraunhofer patterns is constant, showing no temperature dependence of the screening currents or effective areas of the Josephson junctions. Note: the X-axis of the 1.05K plot is half the range of the previous plots.

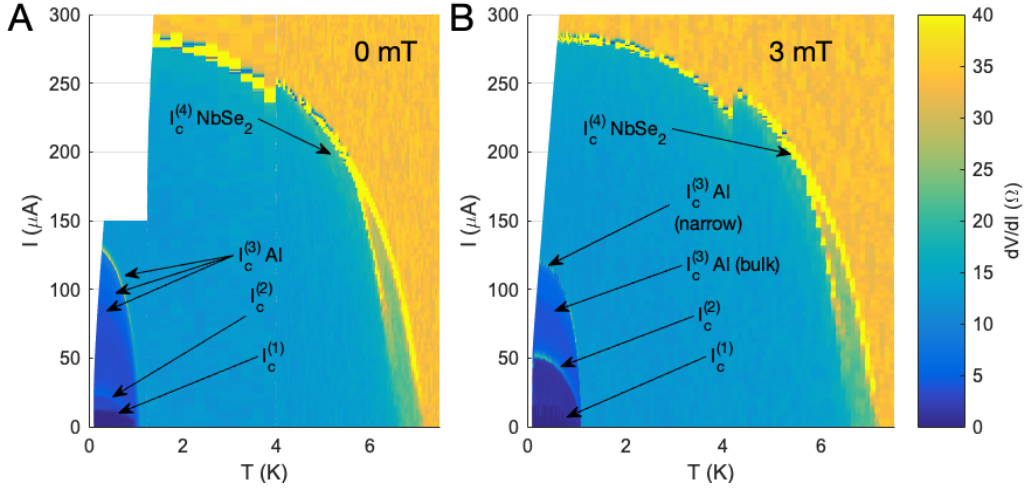


FIG. S5. (A) Plot of dV/dI vs. I_{DC} and T at 0mT (Device F). The critical currents associated with the contacts are well below their maximum at zero flux, indicating that this measurement with zero applied field is measuring a finite amount of trapped flux through the NbSe₂ flake in the areas associated with each junction. (B) Plot of I_{DC} and T vs. dV/dI at 3mT. The smaller of the critical currents (associated with the narrower of the 2 contacts) exhibits hopping behavior between two discrete flux states. This suggests that a single vortex is moving in and out of the area of the NbSe₂ flake measured by this contact. The shift in I_c between the two levels is significant. In both plots, the T_c of all critical currents associated with the aluminum leads and Al/NbSe₂ contacts is 1.2 K. Above 5.5 K the NbSe₂ critical current splits into two critical currents with $T_c = 6.5$ K, 7 K Note: Discontinuity in I_c^4 (NbSe₂) at 4K is attributed to the different heating behavior of the cryogen free dilution refrigerator above and below 4K

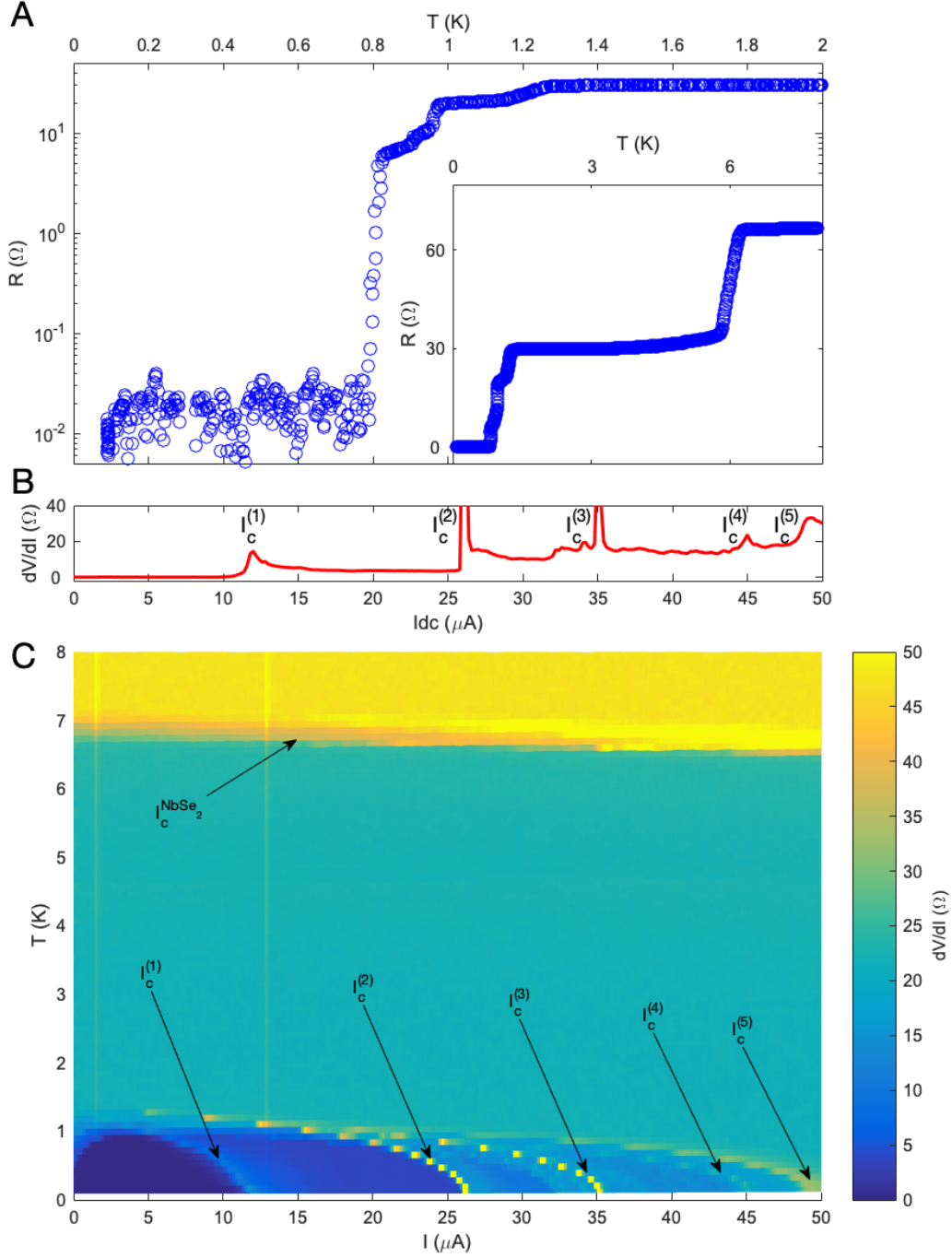


FIG. S6. Zero-resistance contact between few-layer NbSe₂ and aluminum in Device A. **(A)** Semilogarithmic plot of $R(T)$ showing a zero-resistance state limited by the noise floor of roughly 30 m Ω , in sample A. Inset (bottom-right): linear plot of $R(T)$ showing NbSe₂ and multiple Al and Al/NbSe₂ transitions. NbSe₂ is approximately 1.5 $\mu m \times 4 \mu m$ and 12 nm thick (see Table I). **(B)** Differential resistance (dV/dI) vs. DC current I_{DC} of same device, showing five DC critical currents 1,2,3,4,5 with $I_c \approx 12, 26, 35, 45, 49 \mu A$. The temperature dependence of these critical currents in Fig. S6C associates them with aluminum and the Al-NbSe₂ contacts instead of the NbSe₂ flake, the critical current of which is not shown. **(C)** I_{DC} and T vs. dV/dI shows that all five critical currents observed in B are associated with the Al/NbSe₂ contacts and Al leads, as evidenced by $I_c^{(1-5)} \rightarrow 0$ at $T_c^{Al} = 1.2 K$, while $I_c^{NbSe_2} \rightarrow 0$ at bulk $T_c^{NbSe_2} = 7 K$

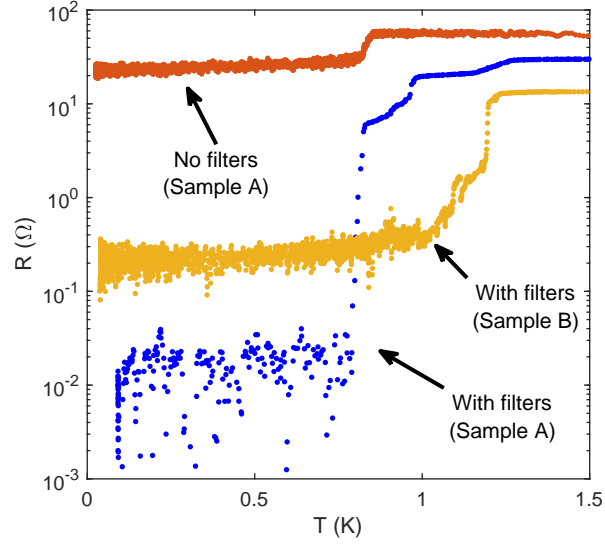


FIG. S7. Comparison of $R(T)$ plots of devices A and B with and without filters used in the measurement. The curve from Fig. S6 is reproduced and compared with a measurement on the same sample without the RC low-pass filters. An $R(T)$ for the SQUID sample with all filters in place shows a residual resistance less than half that of the previous sample without the RC low-pass filter. While we cannot localize the origin of this resistance in this device, we believe that this small residual resistance is negligible with regard to the performance of the SQUID as a superconducting device.

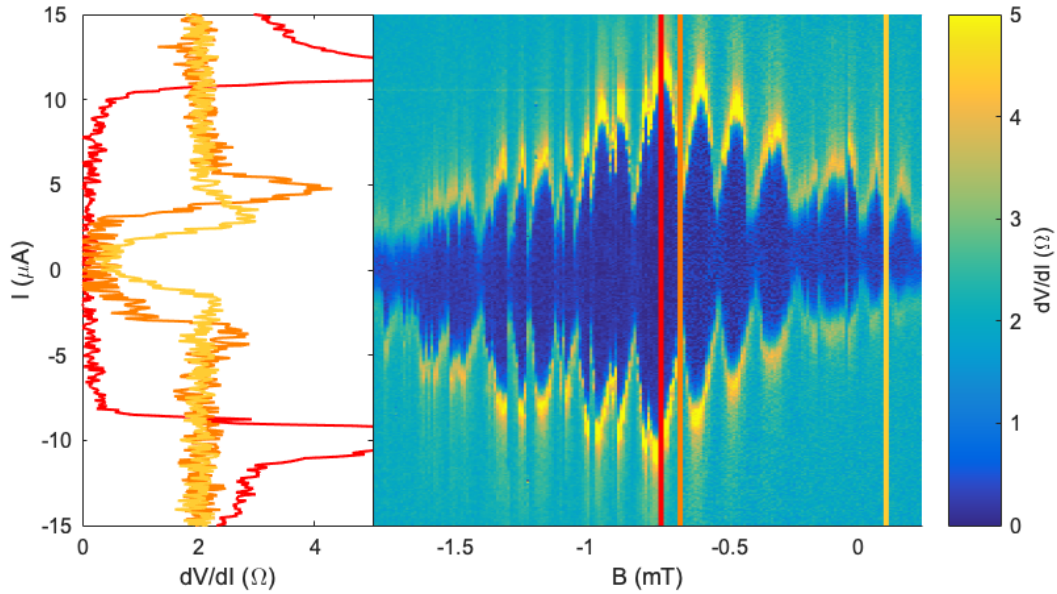


FIG. S8. dV/dI vs. I_{DC} and B (device B), with several representative linecuts. This SQUID device shows a zero resistance state, unlike the quantum interference pattern shown in 3B where a residual resistance was subtracted out. The pattern is offset from zero applied field and multiple discontinuities in the interference pattern are present between -0.7 mT and -1.6 mT, providing evidence of vortex motion in and out of the region inside the NbSe₂ flake associated with the flux response of the SQUID.